Science Advances
AAAS

Supplementary Materials for

Mesozoic intraoceanic subduction shaped the lower mantle beneath the East Pacific Rise

Jingchuan Wang *et al.*

Corresponding author: Jingchuan Wang, jingchuan@ualberta.ca; Rongzhi Lin, rongzhi@ualberta.ca

Sci. Adv. **10**, eado1219 (2024)
DOI: 10.1126/sciadv.ado1219

This PDF file includes:

Supplementary Texts S1 to S3
Figs. S1 to S15
References

Supplementary Text

S1. Plate reconstruction of SE Pacific in the Paleozoic

Prior to the Mesozoic, two major tectonic events occurred in the present-day SE Pacific: the subduction-induced closure of the Rheic Ocean and the subduction of proto-Pacific (Panthalassa) beneath western Gondwana (*30*, *31*). Paleomagnetic and geochronological data reveal that the Rheic Ocean closure occurred during the Devonian-Carboniferous period (420–370 Ma) as the Laurussia supercontinent drifted southward and collided with western Gondwana (*77*, *78*) (fig. S9, A and B). Panthalassa was subsequently subducted along an intraoceanic boundary due to the extension of the Laurussia Plate, starting approximately 390 Ma (*30*) ("PP" in fig. S9, C and D). Following the divergence of Laurussia and southern Gondwana, a second subduction zone was formed along the western margin of Gondwana ("WG" in fig. S9, D-G). The closure of the marginal basin between the two subduction zones was coincident with the accretion of South Patagonia onto western Gondwana (*79*, *80*). The western Gondwana trench continued its eastward drift during the Triassic, initiating a retreat at around 200 Ma (fig. S9, G and H). However, the relatively short interval of the subduction of the Rheic Ocean beneath Laurussia ("EL" in fig. S9A) precludes a prolonged slab-mantle interaction that still impacts the mantle transition zone (MTZ). The motion of Laurussia relative to Gondwana is also subject to considerable uncertainty. In addition, the inferred subduction polarity from seismic tomography is opposite to that of the Patagonian Plate or the western Gondwana subduction zone, thus ruling out its association with the proposed subduction.

S2. Thermal history modeling

In this study, we associate the observed anomaly beneath the Nazca Plate with an ancient oceanic slab. To assess the long-term behavior of a subducted slab, we model temperature evolution within a slab over time (t) using the 1-D unsteady heat conduction equation (*81*)

$$T(z,t) = \frac{1}{2\sqrt{\pi\kappa t}} \int_{-\infty}^{\infty} T_0(z') e^{-\frac{(z-z')^2}{4\kappa t}} dz' \,, \tag{S1}$$

where $T_0(z)$ represents the 1-D temperature distribution at $t = 0$. We adopt a typical mantle thermal diffusivity (κ) value of $1 \times 10^{-6}\ m^2 \cdot s^{-1}$. Our model assumes a slab with a finite thickness of 100 km and an internal temperature of 1000 K. The mantle temperatures above and below the slab are set to 1600 K and 1800 K, respectively. We solve Eq. (S1) using numerical integration. As the slab equilibrates with the mantle, the temperature anomaly gradually widens, while the temperature within the slab remains lower than the surrounding mantle by approximately 150 K over a period of 200–250 Myr (fig. S11). The modeling results indicate that the thermal feature (manifested as cold temperatures) of the slab persists even after 200 Myr. Assuming that seismic velocity is exclusively temperature-dependent and using a temperature derivative of S velocity of –0.7%/100 K at the base of the MTZ (*82*), we compute a velocity perturbation of +1%, which is in general agreement with the tomographic images.

S3. Slab volume and sinking rate

Published global plate reconstruction models do not include an intraoceanic subduction episode since the Mesozoic in our study region, with the exception of the model proposed by van der Meer et al. (*21*) which was based on mantle tomography. Intracoeanic subduction offers perhaps the simplest explanation for our observations, including a thickened MTZ and fast velocity anomalies in tomographic images. To support our interpretation in terms of plate tectonic history, we further investigate the radial distribution of the tomographic anomalies. We use the cross-sectional area method of Hafkenscheid et al. (*83*) to quantify the volume of the "slab" anomaly (fig. S12). The slab edge is defined based on a dV_S cutoff value of +0.4% (see Fig. 3C). The estimated slab volume, as quantified by the cross-sectional area of tomographic anomalies, shows a large peak at ~2100 km depth (fig. S12B). The area-depth curve is also characterized by a slight increase from 500 km to 800 km depth, while the slab volume remains relatively small in the lower mantle across the depth range of 1000–1800 km. The curve also shows that approximately 14% of the total slab volume is still confined within the MTZ.

Global correlations between subduction time and depth (*35, 36, 84*) would suggest that the SPS slab started subduction in the early Triassic and ended in the Cenozoic, a much later termination than that we propose. We compare the depth-dependent trend of slab volume with that of the slab volume flux (total volume consumed at subduction zones per unit time) according to East et al. (*85*) (fig. S12A), which is derived from the global plate reconstruction model of Müller et al. (*86*). We convert the slab flux from time to depth, assuming a constant slab sinking rate. The comparison shows that the globally averaged sinking rate of 1.2–1.3 cm/yr (*35, 36*) does not fully account for the observed depth trend of the slab volume, in particular the excess in the MTZ and the lowermost mantle, as highlighted by a moderate anticorrelation (with a correlation coefficient of −0.42) between the two curves (fig. S12B). This discrepancy indicates depth-varying slab sinking rates. One plausible scenario suggests that the slab encountered resistance to sinking at the base of the MTZ. A time span of around 250 Myr for the subducted material to have reached and piled up at depths of 2000–2500 km corresponds to a lower mantle sinking rate of 1 cm/yr. The presence of slab remnants within the MTZ since the mid-Cretaceous translates to an upper mantle sinking velocity of approximately 0.5 cm/yr. This decelerated upper mantle sinking is consistent with the scenario of long-term slab stagnation.

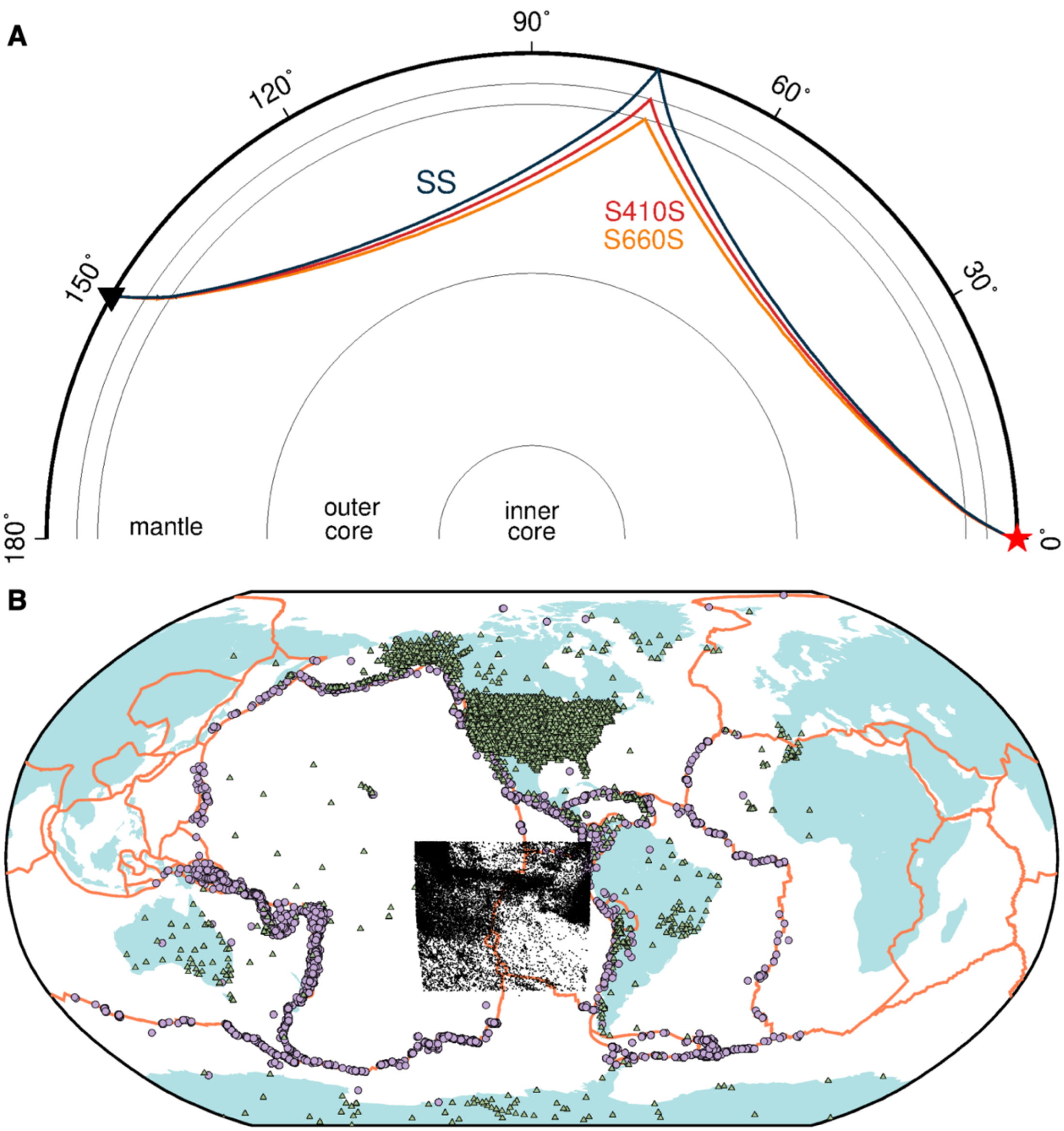

Fig. S1. Map of earthquakes, stations, and bounce points. (**A**) Theoretical raypaths of SS and its precursors for a source-receiver distance of 150°. (**B**) Geographic distribution of the earthquakes (purple circles) and seismic stations (green triangles) used in this study and locations of SS bounce points (black dots). Plate boundaries (*73*) are marked as orange curves.

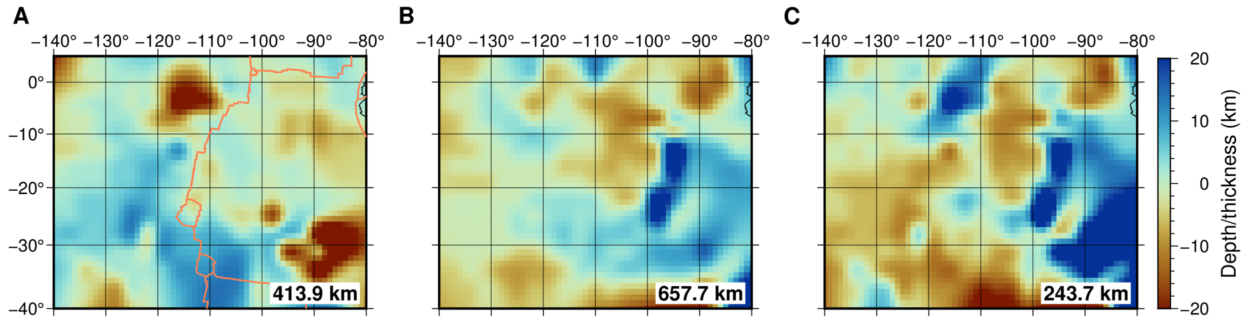

Fig. S2. MTZ topography obtained using the conventional common midpoint stacking method. (**A** to **C**) Topography of the 410 (A), the 660 (B), and MTZ thickness (C). The depth estimates are shown relative to the regional average values at the bottom right corner of each panel. The orange lines in (A) denote the plate boundaries (*73*).

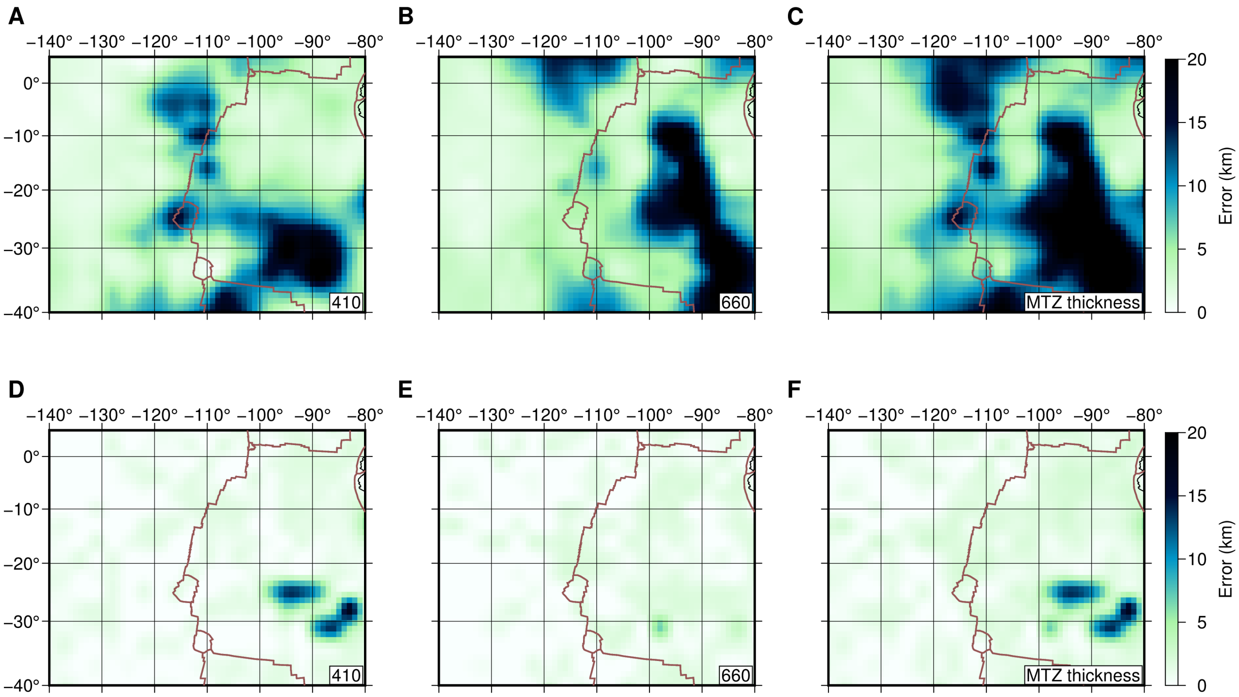

Fig. S3. Maps of standard errors. (**A** to **C**) Standard errors of the 410 depth (A), the 660 depth (B), and the MTZ thickness (C) obtained from the conventional common midpoint stacking. (**D** to **F**) Standard errors of the 410 depth (D), the 660 depth (E), and the MTZ thickness (F) after processing using partial stacking and FMSSA reconstruction.

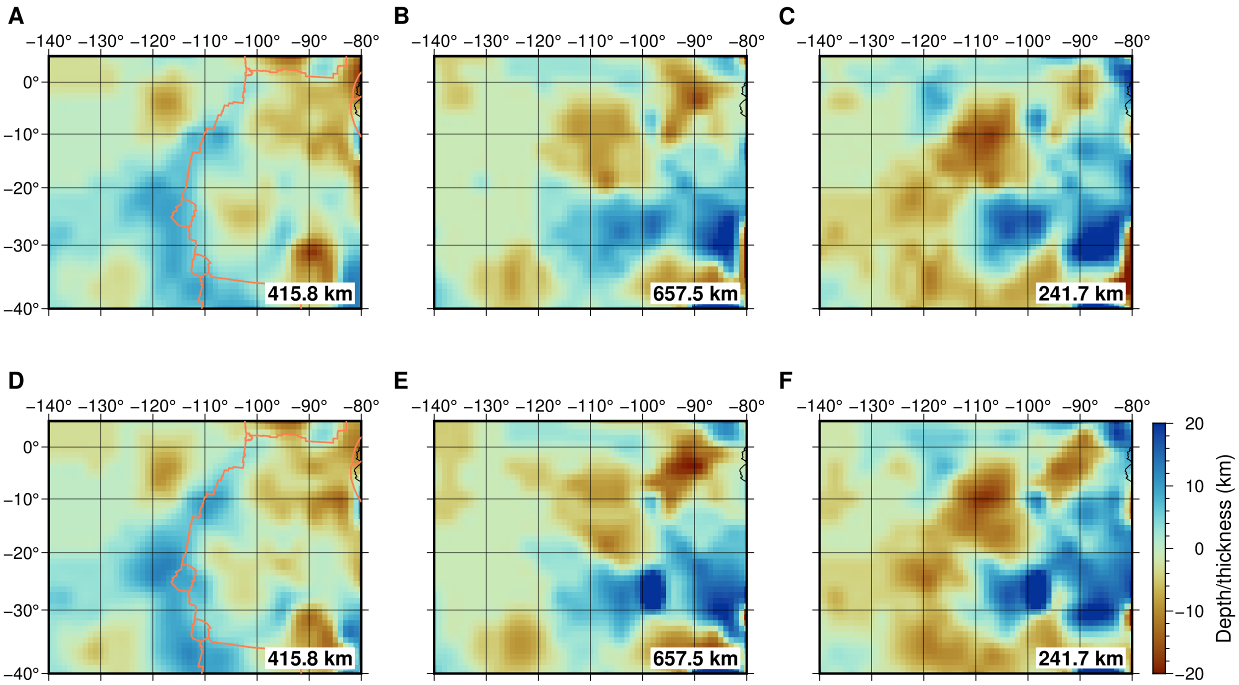

Fig. S4. MTZ topography of the study region using different *k* (data rank threshold) values in the FMSSA reconstruction. (**A** to **C**) Lateral variations in the 410 depth (A), the 660 depth (B), and the MTZ thickness (C) using $k = 85$. (**D** to **F**) Lateral variations in the 410 depth (D), the 660 depth (E), and the MTZ thickness (F) using $k = 120$.

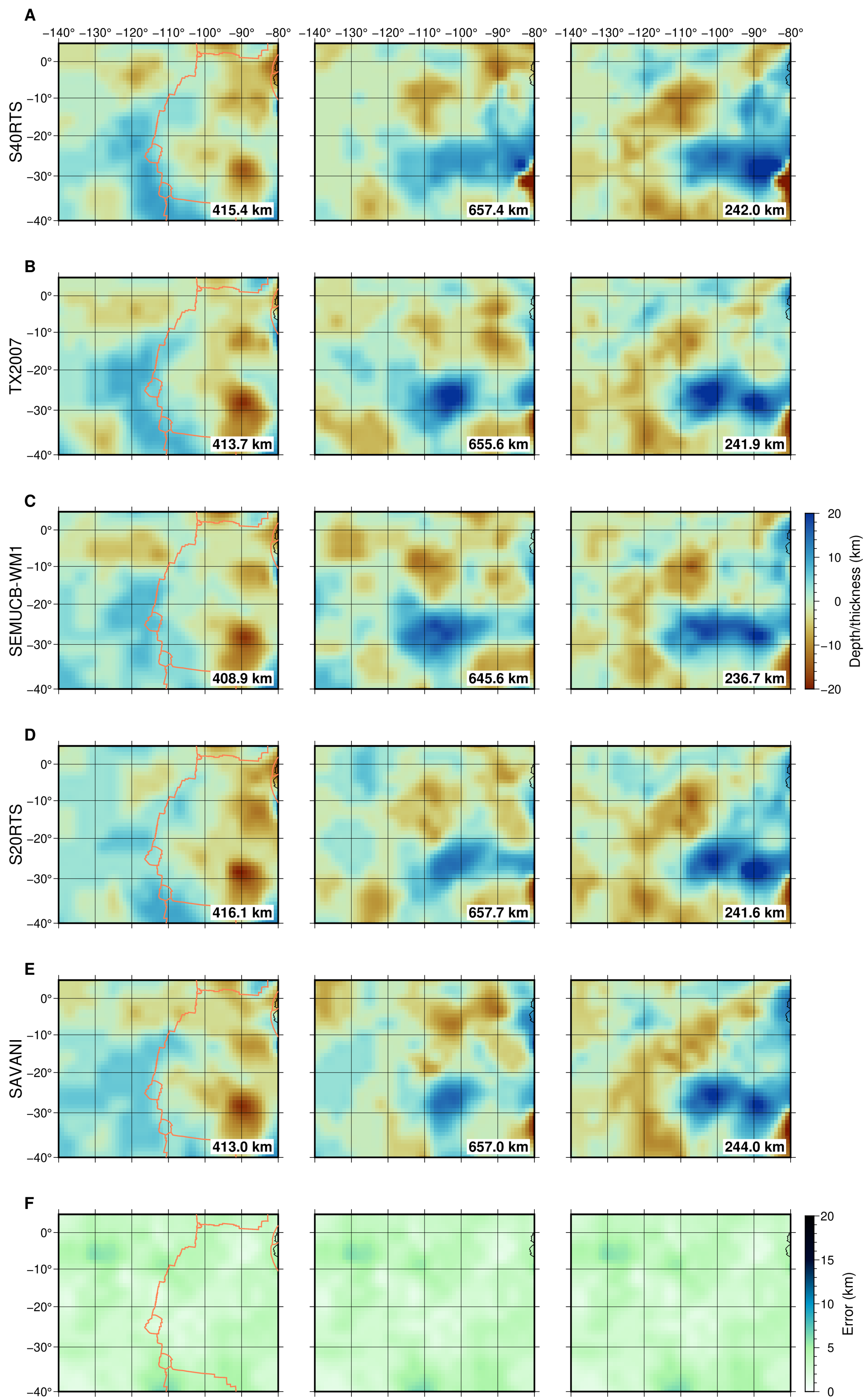
A
B
C
D
E
F
S40RTS
TX2007
SEMUCB-WM1
S20RTS
SAVANI
−140° −130° −120° −110° −100° −90° −80°
0°
−10°
−20°
−30°
−40°
415.4 km
657.4 km
242.0 km
413.7 km
655.6 km
241.9 km
408.9 km
645.6 km
236.7 km
416.1 km
657.7 km
241.6 km
413.0 km
657.0 km
244.0 km
Depth/thickness (km)
20
10
0
−10
−20
Error (km)
20
15
10
5
0

Fig. S5. MTZ topography obtained using different tomographic models for mantle velocity correction. The discontinuity depths and MTZ thickness are shown relative to their regional average values. Maps are shown for models (**A**) S40RTS (*65*), (**B**) TX2007 (*87*), (**C**) SEMUCB-WM1 (*15*), (**D**) S20RTS (*88*), and (**E**) savani (*69*). Panel (A) corresponds to Panels (A) to (C) in Fig. 2. (**F**) The standard deviation of the estimates for the above five models. The orange lines denote the plate boundaries (*73*).

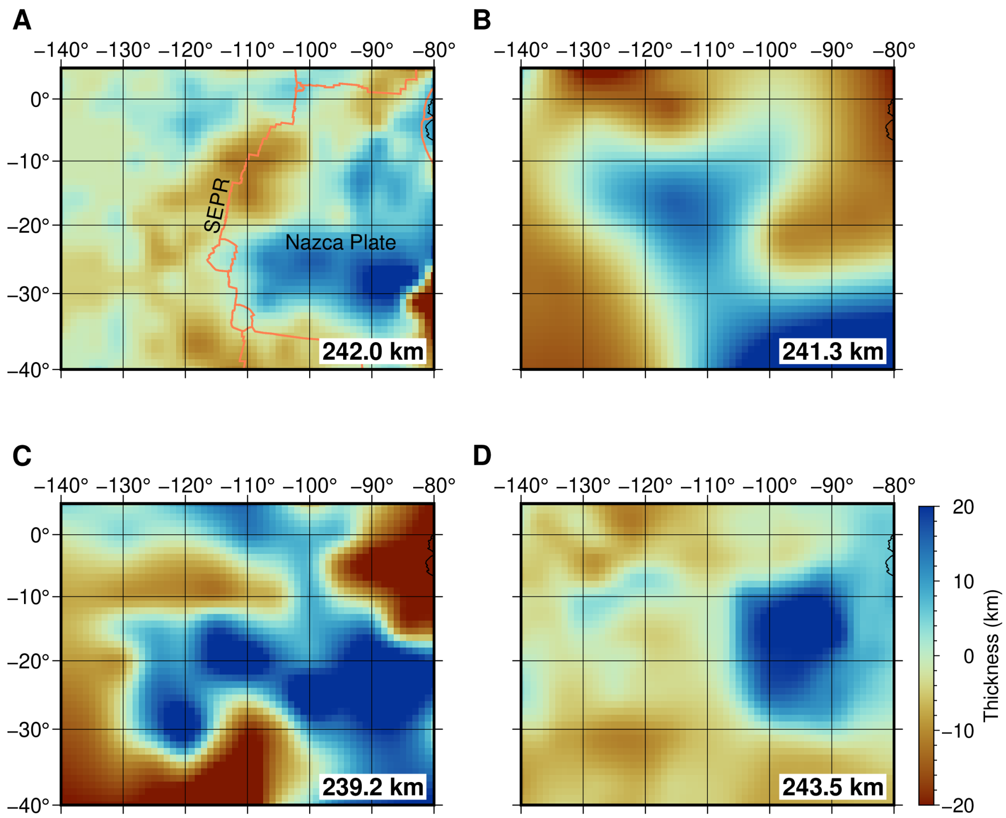

Fig. S6. Comparison of MTZ topography. MTZ thickness models from (**A**) this study, (**B**) Flanagan and Shearer (*26*), (**C**) Houser (*27*), and (**D**) Waszek et al. (*28*). Note that the other three models are global-scale. The average thickness estimates are shown at the bottom right corner of each panel.

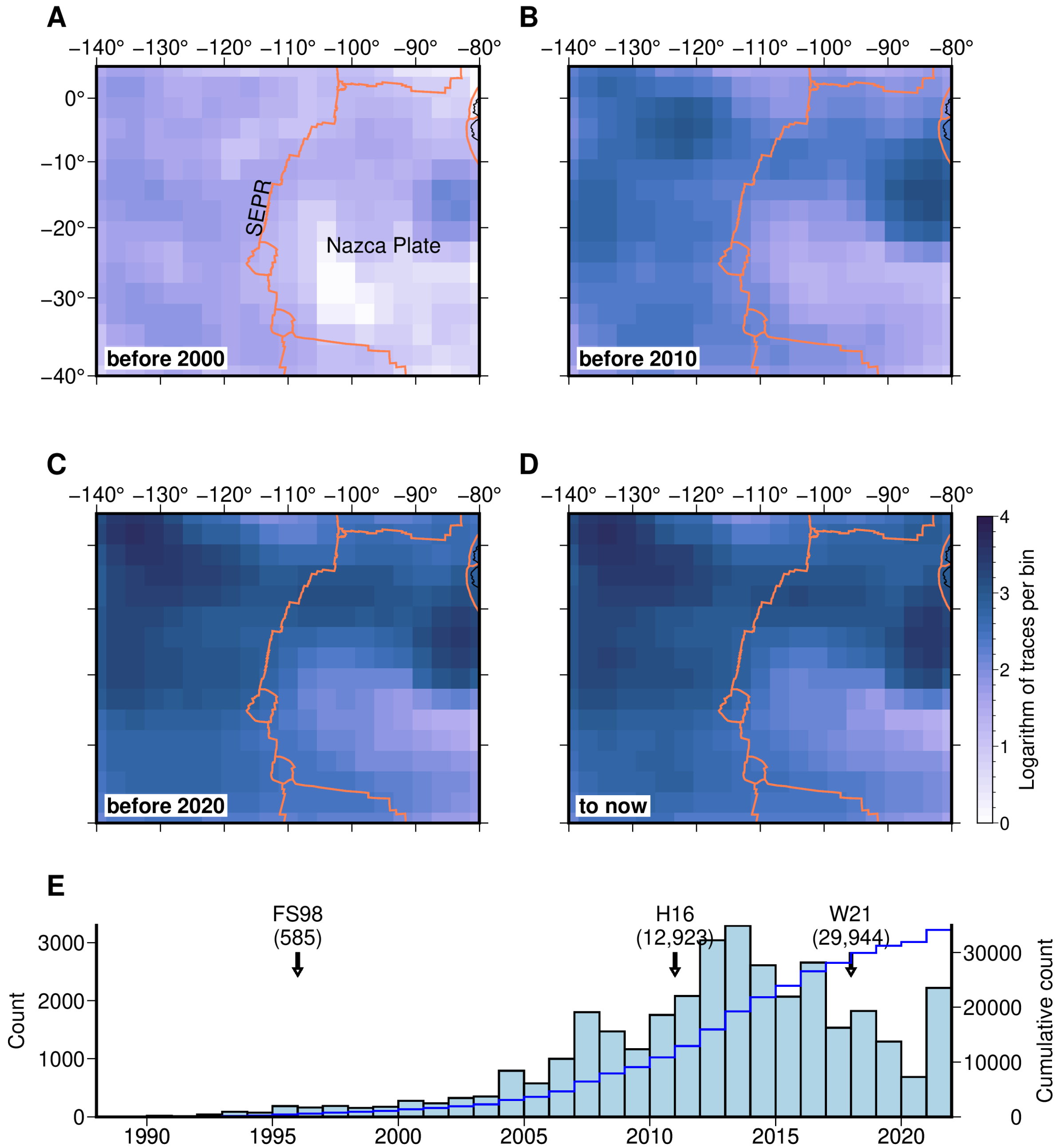

Fig. S7. Precursor data coverage. (**A** to **D**) Logarithmic hit count patterns (number of traces per bin) from precursor data recorded before 2000 (A), before 2010 (B), before 2020 (C), and up to now (D). (**E**) Histogram of the precursor measurements used in this study by year. The blue curve shows the cumulative sum. The end times used by Flanagan and Shearer (*26*) (FS98), Houser (*27*) (H16), and Waszek et al. (*28*) (W21) are marked. The numbers in parentheses indicate the count of measurements available by the completion of each major study, based on the dataset used in this study. Our dataset spans 34 years, but most of our data come from the last decade.

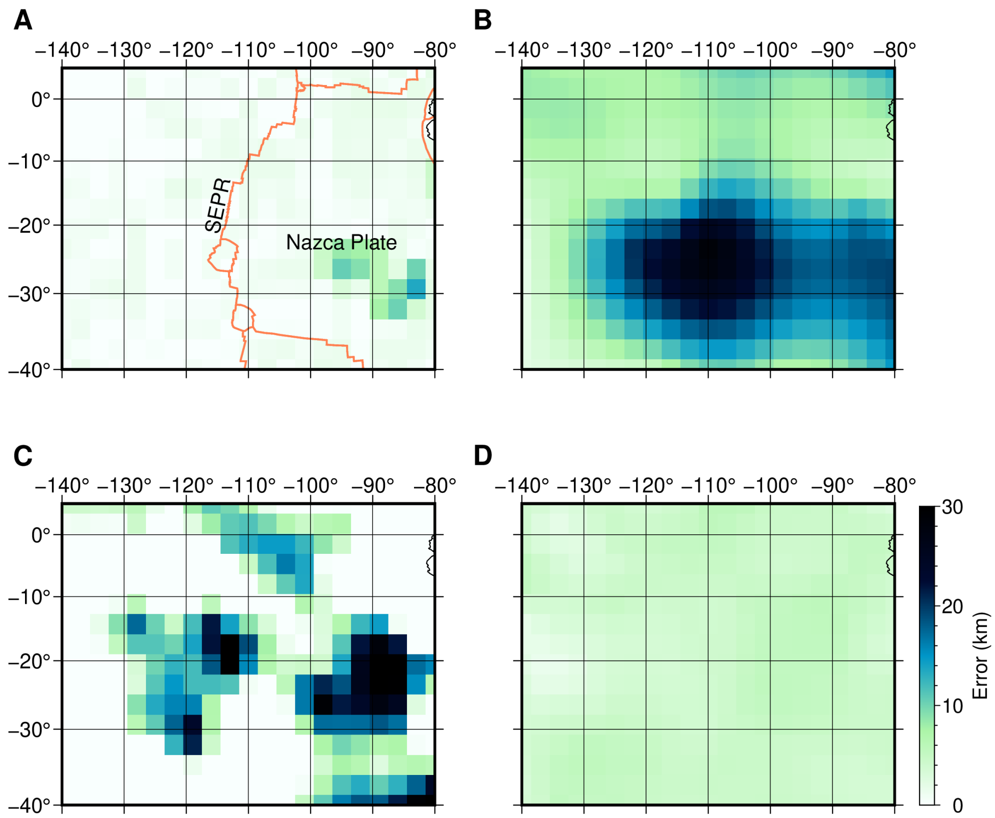

Fig. S8. Comparison of MTZ topography errors. Maps of the errors in MTZ thickness from (**A**) this study, (**B**) Flanagan and Shearer (*26*), (**C**) Houser (*27*), and (**D**) Waszek et al. (*28*).

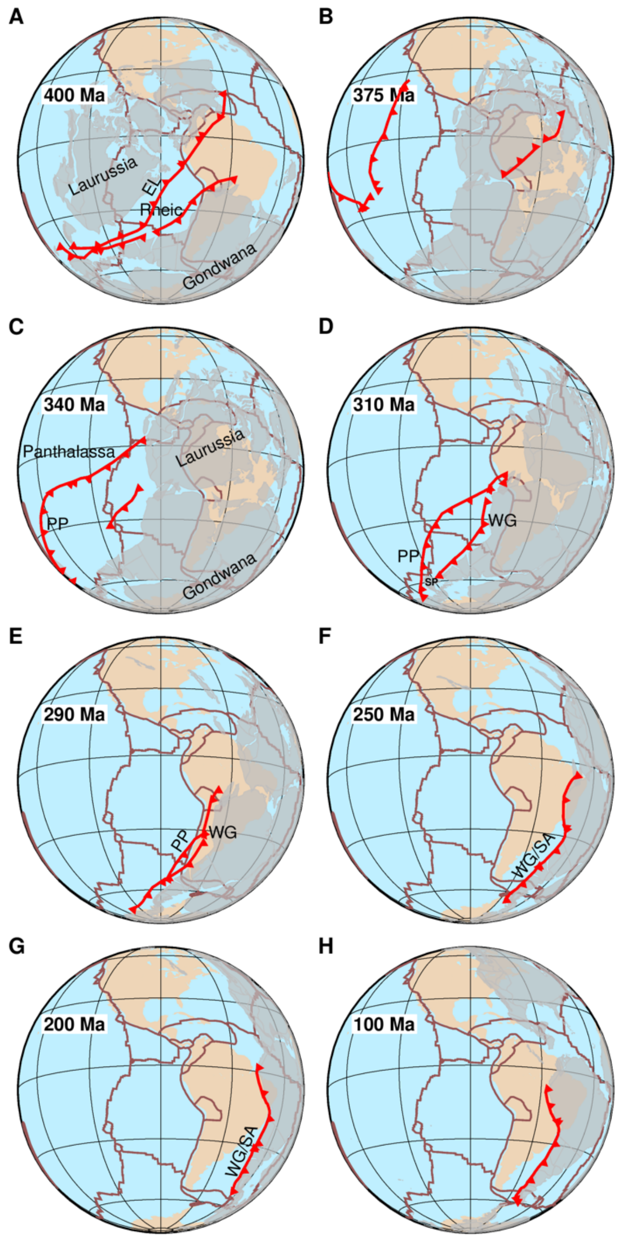

Fig. S9. Modeled subduction zones in the study region since 400 Ma from Matthews et al. (*31*). The gray shades are the reconstructed plates, and the orange shades indicate the present-day continental plates. The thick brown lines indicate the present-day plate boundaries (*73*). (**A** and **B**) During the Devonian, the Rheic Ocean subducted along East Laurussia (EL) and western Gondwana, and the Laurussia supercontinent drifted southward and collided with western Gondwana. (**C** to **H**) Plate reconstructions of the Patagonian Plate (PP) and the western Gondwana (WG) subduction zones at (C) 340 Ma, (D) 310 Ma, (E) 290 Ma, (F) 250 Ma, (G) 200 Ma, and (H) 100 Ma (*29*). The retreat of the western Gondwana/South America (WG/SA) trench started at around 200 Ma.

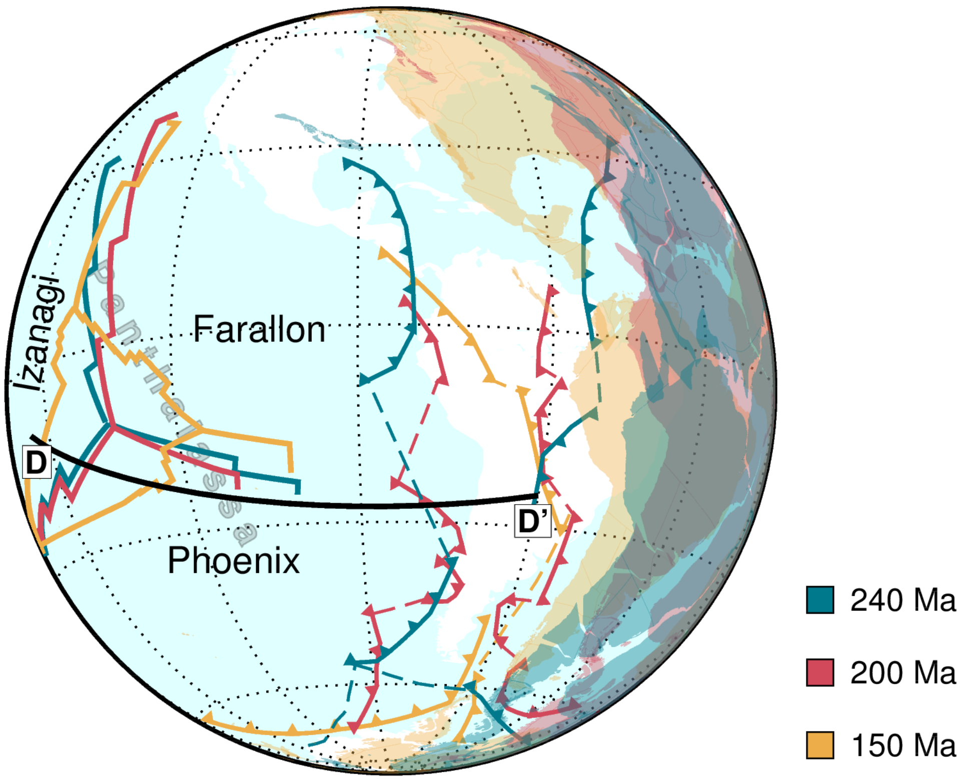

Fig. S10. Plate reconstructions of southern Panthalassa between 240 and 150 Ma. Reconstructions of the Izanagi-Farallon-Phoenix triple junction are obtained from Torsvik et al. (*89*). The colored lines with triangles denote interpreted subduction zones in plate reconstruction model of van der Meer et al. (*21*). The dashed lines represent presumed transform zones. The profile D-D′ show the location of the cross-sectional view of model interpretation in Fig. 5.

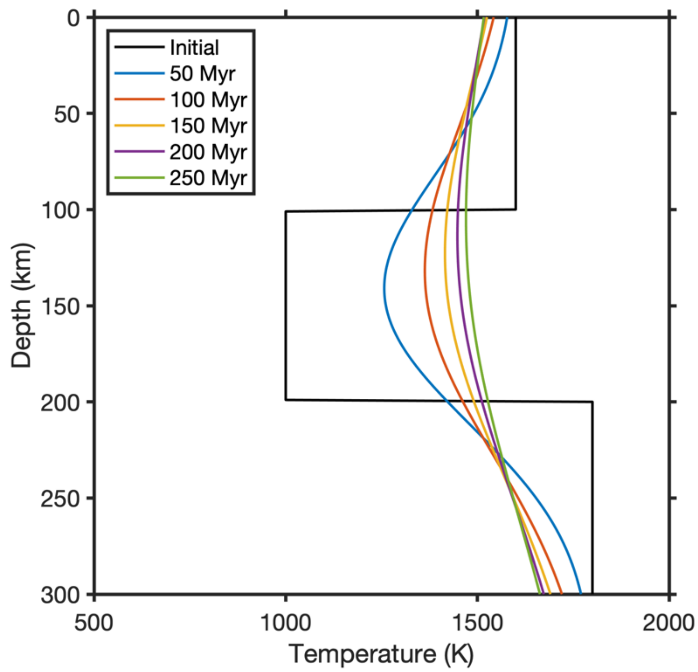

Fig. S11. Modeling of slab temperature growth over a period of 250 Myr. The modeling assumes a 100-km-thick slab with an initial internal temperature of 1000 K (black line). The ambient mantle thermal conditions are 1600 K above the slab and 1800 K below the slab. A thermal diffusivity of $1 \times 10^6\ m^2 \cdot s^{-1}$ is used. Over a period of 200 Myr, the temperature anomaly gradually widens, while the temperature within the slab remains lower than the ambient condition with a deficit of approximately 150 K.

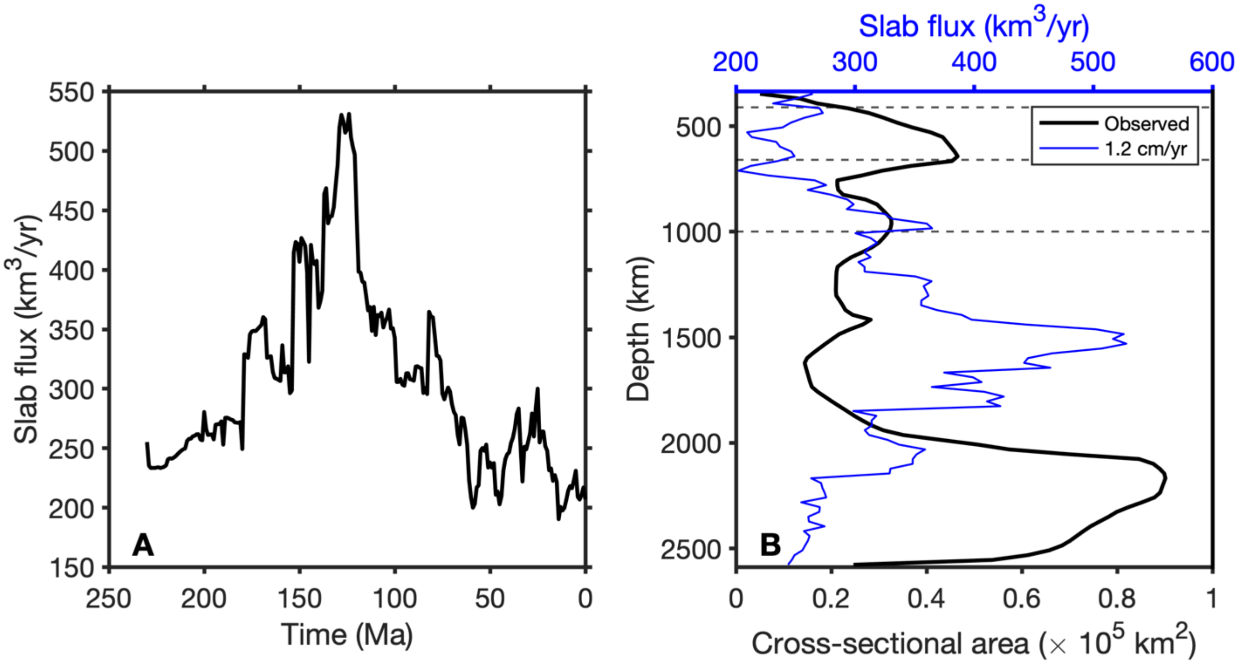

Fig. S12. Comparison of the depth-dependent trend of the SPS slab volume with that of the reported slab flux. (**A**) The global estimate of the slab volume flux (the total slab volume consumed globally at subduction zones per unit time) from East et al. (*85*). (**B**) The solid black curve represents the depth variations in the SPS slab volume [cross-sectional area of tomographic anomalies in the LLNL-G3D-JPS-model (*20*)] (see Fig. 3C). The thin blue curve is the depth-converted slab flux (panel A) assuming a global average slab sinking rate of 1.2 cm/yr. The anti-correlation between the two curves indicates that a constant sinking velocity of 1.2 cm/yr fails to explain the observed slab sinking behavior. The dashed black lines indicate the depths of 410 km, 660 km, and 1000 km.

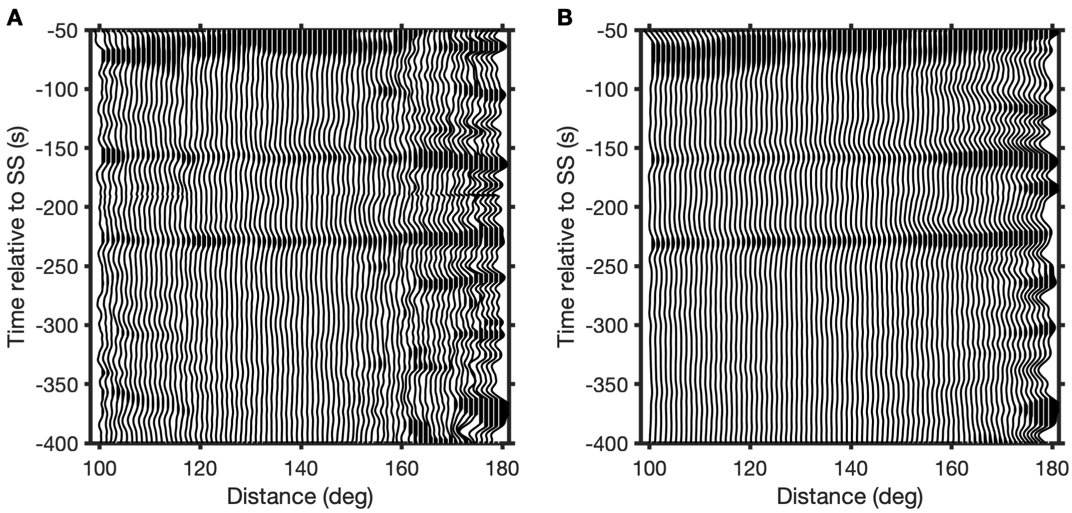

Fig. S13. Example of a common midpoint gather of the observed dataset. (**A**) The raw common midpoint gather. (B) The common midpoint gather after reconstruction and denoising using the FMSSA algorithm. The phases at around 150 s and 230 s prior to SS correspond to S410S and S660S precursors.

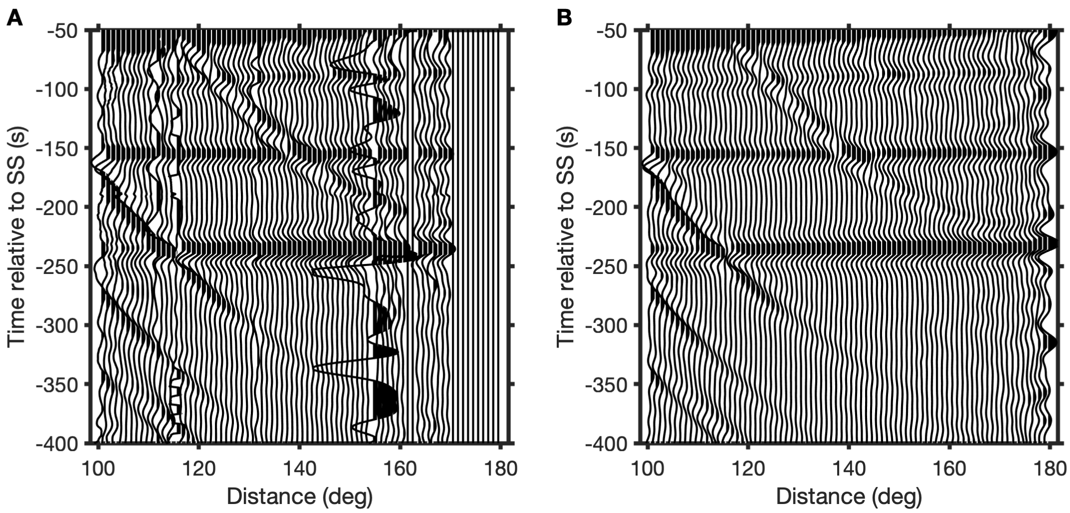

Fig. S14. Synthetic test based on the PREM model. (**A**) Decimated synthetic data with 10% traces missing and corrupted traces. (**B**) Reconstructed and denoised data using the FMSSA algorithm.

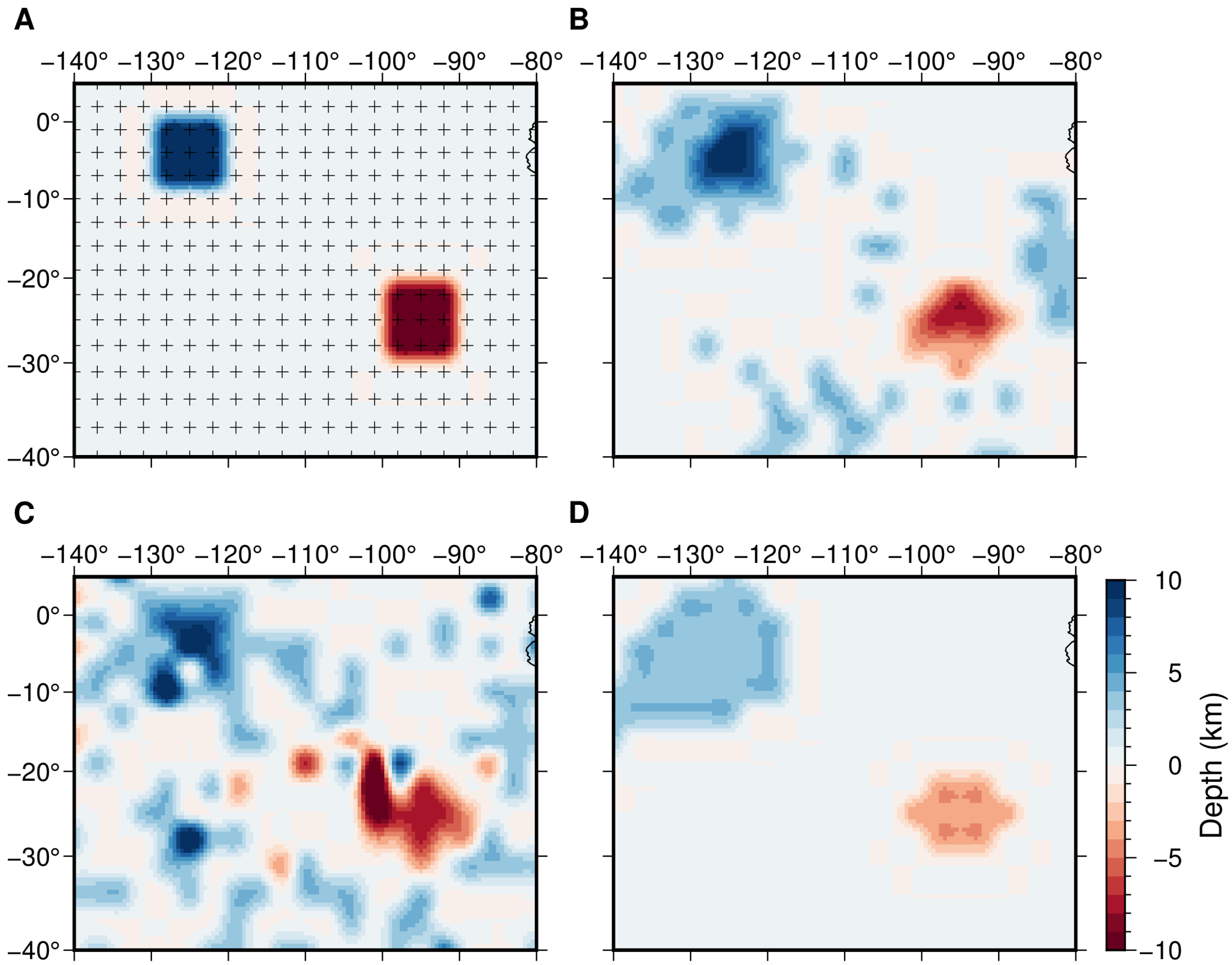

Fig. S15. Spike test. (**A**) Input topography model. (**B**) Output model from the common midpoint stacking of noise-free traces using the actual SS midpoint distribution (i.e., source-receiver geometry). (**C**) Same as (B) but with 10% random Gaussian noise, and 10% of the total traces are also contaminated with non-Gaussian erratic noise. (**D**) Resulting model after FMSSA reconstruction of the noisy data in (C).

REFERENCES AND NOTES

1. W. Su, R. L. Woodward, A. M. Dziewonski, Degree 12 model of shear velocity heterogeneity in the mantle. *J. Geophys. Res. Solid Earth* **99**, 6945–6980 (1994).

2. M. Ishii, J. Tromp, Normal-mode and free-air gravity constraints on lateral variations in velocity and density of Earth's mantle. *Science* **285**, 1231–1236 (1999).

3. Y. J. Gu, A. M. Dziewonski, W. Su, G. Ekström, Models of the mantle shear velocity and discontinuities in the pattern of lateral heterogeneities. *J. Geophys. Res. Solid Earth* **106,** 11169–11199 (2001).

4. E. J. Garnero, A. K. McNamara, Structure and dynamics of Earth's lower mantle. *Science* **320**, 626–628 (2008).

5. F. Deschamps, L. Cobden, P. J. Tackley, The primitive nature of large low shear-wave velocity provinces. *Earth Planet. Sci. Lett.* **349**, 198–208 (2012).

6. M. D. Ballmer, C. Houser, J. W. Hernlund, R. M. Wentzcovitch, K. Hirose, Persistence of strong silica-enriched domains in the Earth's lower mantle. *Nat. Geosci.* **10**, 236–240 (2017).

7. A. M. Dziewonski, V. Lekic, B. A. Romanowicz, Mantle anchor structure: An argument for bottom up tectonics. *Earth Planet. Sci. Lett.* **299**, 69–79 (2010).

8. S. Ni, E. Tan, M. Gurnis, D. Helmberger, Sharp sides to the African superplume. *Science* **296**, 1850–1852 (2002).

9. Y. He, L. Wen, Structural features and shear-velocity structure of the "Pacific anomaly". *J. Geophys. Res. Solid Earth* **114**, B02309 (2009).

10. A. McNamara, S. Zhong, Thermochemical structures beneath Africa and the Pacific Ocean. *Nature* **437**, 1136–1139 (2005).

11. D. J. Bower, M. Gurnis, M. Seton, Lower mantle structure from paleogeographically constrained dynamic Earth models. *Geochem. Geophys. Geosyst.* **14**, 44–63 (2012).

12. S. Zhong, M. L. Rudolph, On the temporal evolution of long-wavelength mantle structure of the Earth since the early Paleozoic. *Geochem. Geophys. Geosyst.* **16**, 1599–1615 (2015).

13. A. Davaille, B. Romanowicz, Deflating the LLSVPs: Bundles of mantle thermochemical plumes rather than thick stagnant "piles". *Tectonics* **39**, e2020TC006265 (2020).

14. G. Schubert, G. Masters, P. Olson, P. Tackley, Superplumes or plume clusters? *Phys. Earth Planet. Inter.* **146,** 147–162 (2004).

15. S. W. French, B. Romanowicz, Broad plumes rooted at the base of the Earth's mantle beneath major hotspots. *Nature* **525**, 95–99 (2015).

16. S. Cottaar, V. Lekic, Morphology of seismically slow lower-mantle structures. *Geophys. J. Int.* **207**, 1122–1136 (2016).

17. R. Montelli, G. Nolet, F A Dahlen, G. Masters, E. R. Engdahl, S.-H. Hung, Finite-frequency tomography reveals a variety of plumes in the mantle. *Science* **303**, 338–343 (2004).

18. W. Lei, Y. Ruan, E. Bozdağ, D. Peter, M. Lefebvre, D. Komatitsch, J. Tromp, J. Hill, N. Podhorszki, D. Pugmire, Global adjoint tomography—Model GLAD-M25. *Geophys. J. Int.* **223**, 1–21 (2020).

19. A. Deuss, Global observations of mantle discontinuities using SS and PP precursors. *Surv. Geophys.* **30**, 301–326 (2009).

20. N. A. Simmons, S. C. Myers, G. Johannesson, E. Matzel, S. P. Grand, Evidence for long-lived subduction of an ancient tectonic plate beneath the southern Indian Ocean. *Geophys. Res. Lett.* **42**, 9270–9278 (2015).

21. D. G. van der Meer, T. H. Torsvik, W. Spakman, D. J. J. van Hinsbergen, M. L. Amaru, Intra-Panthalassa Ocean subduction zones revealed by fossil arcs and mantle structure. *Nat. Geosci.* **5**, 215–219 (2012).

22. Y. J. Gu, A. M. Dziewonski, Global variability of transition zone thickness. *J. Geophys. Res. Solid Earth* **107**, ESE2-1–ESE 2-17 (2002).

23. Y. Shen, A. F. Sheehan, K. G. Dueker, C. de Groot-Hedlin, H. Gilbert, Mantle discontinuity structure beneath the southern East Pacific Rise from P-to-S converted phases. *Science* **280**, 1232–1235 (1998).

24. C. A. Dalton, C. H. Langmuir, A. Gale, Geophysical and geochemical evidence for deep temperature variations beneath mid-ocean ridges. *Science* **344**, 80–83 (2014).

25. M. R. Agius, C. A. Rychert, N. Harmon, S. Tharimena, J.-M. Kendall, A thin mantle transition zone beneath the equatorial Mid-Atlantic ridge. *Nature* **589**, 562–566 (2021).

26. M. P. Flanagan, P. M. Shearer, Global mapping of topography on transition zone velocity discontinuities by stacking *SS* precursors. *J. Geophys. Res. Solid Earth* **103**, 2673–2692 (1998).

27. C. Houser, Global seismic data reveal little water in the mantle transition zone. *Earth Planet. Sci. Lett.* **448**, 94–101 (2016).

28. L. Waszek, B. Tauzin, N. C. Schmerr, M. D. Ballmer, J. C. Afonso, A poorly mixed mantle transition zone and its thermal state inferred from seismic waves. *Nat. Geosci.* **14**, 949–955 (2021).

29. G. P. Hayes, G. L. Moore, D. E. Portner, M. Hearne, H. Flamme, M. Furtney, G. M. Smoczyk, Slab2, a comprehensive subduction zone geometry model. *Science* **362**, 58–61 (2018).

30. M. Domeier, T. H. Torsvik, Plate tectonics in the late paleozoic. *Geosci. Front.* **5**, 303–350 (2014).

31. K. J. Matthews, K. T. Maloney, S. Zahirovic, S. E. Williams, M. Seton, R. D. Müller, Global plate boundary evolution and kinematics since the late paleozoic. *Glob. Planet. Change* **146**, 226–250 (2016).

32. K. Sigloch, M. G. Mihalynuk, Intra-oceanic subduction shaped the assembly of Cordilleran North America. *Nature* **496**, 50–56 (2013).

33. M. Seton, R. D. Müller, S. Zahirovic, C. Gaina, T. Torsvik, G. Shephard, A. Talsma, M. Gurnis, M. Turner, S. Maus, M. Chandler, Global continental and ocean basin reconstructions since 200Ma. *Earth Sci. Rev.* **113**, 212–270 (2012).

34. Y.-W. Chen, J. Wu, J. Suppe, Southward propagation of Nazca subduction along the Andes. *Nature* **565**, 441–447 (2019).

35. D. G. van der Meer, W. Spakman, D. J. van Hinsbergen, M. L. Amaru, T. H. Torsvik, Towards absolute plate motions constrained by lower-mantle slab remnants. *Nat. Geosci.* **3**, 36–40 (2010).

36. N. P. Butterworth, A. S. Talsma, R. D. Müller, M. Seton, H.-P. Bunge, B. S. A. Schuberth, G. E. Shephard, C. Heine, Geological, tomographic, kinematic and geodynamic constraints on the dynamics of sinking slabs. *J. Geodyn.* **73**, 1–13 (2014).

37. D. J. Weidner, Y. Wang, Chemical- and clapeyron-induced buoyancy at the 660 km discontinuity. *J. Geophys. Res. Solid Earth* **103**, 7431–7441 (1998).

38. V. Thio, L. Cobden, J. Trampert, Seismic signature of a hydrous mantle transition zone. *Phys. Earth Planet. Inter.* **250**, 46–63 (2016).

39. P. Bird, Continental delamination and the colorado plateau. *J. Geophys. Res. Solid Earth* **84**, 7561–7571 (1979).

40. G. A. Houseman, D. P. McKenzie, P. Molnar, Convective instability of a thickened boundary layer and its relevance for the thermal evolution of continental convergent belts. *J. Geophys. Res. Solid Earth* **86**, 6115–6132 (1981).

41. O. H. Göğüş, R. N. Pysklywec, Near-surface diagnostics of dripping or delaminating lithosphere. *J. Geophys. Res. Solid Earth* **113**, B11404 (2008).

42. R. S. Detrick, A. J. Harding, G. M. Kent, J. A. Orcutt, J. C. Mutter, P. Buhl, Seismic structure of the southern East Pacific Rise. *Science* **259**, 499–503 (1993).

43. B. Steinberger, Effects of latent heat release at phase boundaries on flow in the Earth's mantle, phase boundary topography and dynamic topography at the Earth's surface. *Phys. Earth Planet. Inter.* **164**, 2–20 (2007).

44. M. D. Ballmer, N. C. Schmerr, T. Nakagawa, J. Ritsema, Compositional mantle layering revealed by slab stagnation at ~1000-km depth. *Sci. Adv.* **1**, e1500815 (2015).

45. M. L. Rudolph, V. Lekić, C. Lithgow-Bertelloni, Viscosity jump in Earth's mid-mantle. *Science* **350**, 1349–1352 (2015).

46. R. Van der Voo, W. Spakman, H. Bijwaard, Mesozoic subducted slabs under Siberia. *Nature* **397**, 246–249 (1999).

47. E. Tan, W. Leng, S. Zhong, M. Gurnis, On the location of plumes and lateral movement of thermochemical structures with high bulk modulus in the 3-D compressible mantle. *Geochem. Geophys. Geosyst.* **12**, Q07005 (2011).

48. Q. Yuan, M. Li, Vastly different heights of LLVPs caused by different strengths of historical slab push. *Geophys. Res. Lett.* **49**, e2022GL099564 (2022).

49. N. A. Simmons, A. M. Forte, L. Boschi, S. P. Grand, GyPSuM: A joint tomographic model of mantle density and seismic wave speeds. *J. Geophys. Res. Solid Earth* **115**, 2010JB007631 (2010).

50. F. Deschamps, P. J. Tackley, Searching for models of thermo-chemical convection that explain probabilistic tomography: I. Principles and influence of rheological parameters. *Phys. Earth Planet. Inter.* **171**, 357–373 (2008).

51. F. Deschamps, P. J. Tackley, Searching for models of thermo-chemical convection that explain probabilistic tomography. II—Influence of physical and compositional parameters. *Phys. Earth Planet. Inter.* **176**, 1–18 (2009).

52. L. H. Kellogg, B. H. Hager, R. D. van der Hilst, Compositional stratification in the deep mantle. *Science* **283**, 1881–1884 (1999).

53. G. Gianni, C. Navarrete, D. Orts, J. Tobal, A. Folguera, M. Giménez, Patagonian broken foreland and related synorogenic rifting: The origin of the chubut group basin. *Tectonophysics* **649**, 81–99 (2015).

54. A. M. Dziewonski, D. L. Anderson, Preliminary reference Earth model. *Phys. Earth Planet. Inter.* **25**, 297–356 (1981).

55. Y. J. Gu, M. Sacchi, Radon transform methods and their applications in mapping mantle reflectivity structure. *Surv. Geophys.* **30**, 327–354 (2009).

56. R. Schultz, Y. J. Gu, Multiresolution imaging of mantle reflectivity structure using SS and P′P′ precursors. *Geophys. J. Int.* **195**, 668–683 (2013).

57. V. Oropeza, M. Sacchi, Simultaneous seismic data denoising and reconstruction via multichannel singular spectrum analysis. *Geophysics* **76**, V25–V32 (2011).

58. A. E. Beaton, J. W. Tukey, The fitting of power series, meaning polynomials, illustrated on band-spectroscopic data. *Technometrics* **16**, 147–185 (1974).

59. F. Carozzi, M. D. Sacchi, Interpolated multichannel singular spectrum analysis: A reconstruction method that honors true trace coordinates. *Geophysics* **86**, V55–V70 (2021).

60. R. Lin, Y. Guo, F. Carozzi, M. D. Sacchi, Simultaneous deblending and source reconstruction for compressive 3D simultaneous-source acquisition data via interpolated multichannel singular spectrum analysis. *Geophysics* **87**, V559–V570 (2022).

61. R. Lin, B. Bahia, M. D. Sacchi, Iterative deblending of simultaneous-source seismic data via a robust singular spectrum analysis filter. *IEEE Trans. Geosci. Remote Sens.* **60**, 1–10 (2021).

62. J. Cheng, M. Sacchi, J. Gao, Computational efficient multidimensional singular spectrum analysis for prestack seismic data reconstruction. *Geophysics* **84**, V111–V119 (2019).

63. K. Fuchs, G. Müller, Computation of synthetic seismograms with the reflectivity method and comparison with observations. *Geophys. J. Int.* **23**, 417–433 (1971).

64. G. Laske, G. Masters, Z. Ma, M. Pasyanos, Update on CRUST1.0 - A 1-degree global model of Earth's crust. *Geophys. Res. Abstr.* **15**, 2658 (2013).

65. J. Ritsema, A. A. Deuss, H. J. van Heijst, J. H. Woodhouse, S40RTS: A degree-40 shear-velocity model for the mantle from new Rayleigh wave dispersion, teleseismic traveltime and normal-mode splitting function measurements. *Geophys. J. Int.* **184**, 1223–1236 (2011).

66. B. Efron, R. Tibshirani, Statistical data analysis in the computer age. *Science* **253**, 390–395 (1991).

67. G. E. Shephard, C. Houser, J. W. Hernlund, J. J. Valencia-Cardona, R. G. Trønnes, R. M. Wentzcovitch, Seismological expression of the iron spin crossover in ferropericlase in the Earth's lower mantle. *Nat. Commun.* **12**, 5905 (2021).

68. P. Moulik, G. Ekström, An anisotropic shear velocity model of the Earth's mantle using normal modes, body waves, surface waves and long-period waveforms. *Geophys. J. Int.* **199**, 1713–1738 (2014).

69. L. Auer, L. Boschi, T. W. Becker, T. Nissen-Meyer, D. Giardini, *Savani*: A variable resolution whole-mantle model of anisotropic shear velocity variations based on multiple data sets. *J. Geophys. Res. Solid Earth* **119**, 3006–3034 (2014).

70. A. Tesoniero, L. Auer, L. Boschi, F. Cammarano, Hydration of marginal basins and compositional variations within the continental lithospheric mantle inferred from a new global model of shear and compressional velocity. *J. Geophys. Res. Solid Earth* **120**, 7789–7813 (2015).

71. C. Lu, S. P. Grand, H. Lai, E. J. Garnero, TX2019slab: A new *P* and *S* tomography model incorporating subducting slabs. *J. Geophys. Res. Solid Earth* **124**, 11549–11567 (2019).

72. T. W. Becker, A. J. Schaeffer, S. Lebedev, C. P. Conrad, Toward a generalized plate motion reference frame. *Geophys. Res. Lett.* **42**, 3188–3196 (2015).

73. P. Bird, An updated digital model of plate boundaries. *Geochem. Geophys. Geosyst.* **4**, 1027 (2003).

74. M. Seton, R. D. Müller, S. Zahirovic, S. Williams, N. M. Wright, J. Cannon, J. M. Whittaker, K. J. Matthews, R. McGirr, A global data set of present-day oceanic crustal age and seafloor spreading parameters. *Geochem. Geophys. Geosyst.* **21**, e2020GC009214 (2020).

75. V. Lekic, S. Cottaar, A. Dziewonski, B. Romanowicz, Cluster analysis of global lower mantle tomography: A new class of structure and implications for chemical heterogeneity. *Earth Planet. Sci. Lett.* **357**, 68–77 (2012).

76. J. B. Murphy, J. D. Keppie, R. D. Nance, J. Dostal, Comparative evolution of the iapetus and rheic oceans: A North America perspective. *Gondw. Res.* **17**, 482–499 (2010).

77. R. D. Nance, G. Gutiérrez-Alonso, J. D. Keppie, U. Linnemann, J. B. Murphy, C. Quesada, R. A. Strachan, N. H. Woodcock, Evolution of the rheic ocean. *Gondw. Res.* **17**, 194–222 (2010).

78. H. Bahlburg, F. Hervé, Geodynamic evolution and tectonostratigraphic terranes of northwestern Argentina and northern Chile. *Geol. Soc. Am. Bull.* **109**, 869–884 (1997).

79. V. A. Ramos, Patagonia: A paleozoic continent adrift? *J. South Am. Earth Sci.* **26**, 235–251 (2008).

80. D. Turcotte, G. Schubert, "Heat transfer" in *Geodynamics* (Cambridge Univ. Press, ed. 3, 2014), pp. 160–229.

81. F. Cammarano, S. Goes, P. Vacher, D. Giardini, Inferring upper-mantle temperatures from seismic velocities. *Phys. Earth Planet. Inter.* **138,** 197–222 (2003).

82. E. Hafkenscheid, M. J. R. Wortel, W. Spakman, Subduction history of the Tethyan region derived from seismic tomography and tectonic reconstructions. *J. Geophys. Res. Solid Earth* **111**, B08401 (2006).

83. D. G. van der Meer, D. J. J. van Hinsbergen, W. Spakman, Atlas of the underworld: Slab remnants in the mantle, their sinking history, and a new outlook on lower mantle viscosity. *Tectonophysics* **723**, 309–448 (2018).

84. M. East, R. D. Müller, S. Williams, S. Zahirovic, C. Heine, Subduction history reveals cretaceous slab superflux as a possible cause for the mid-cretaceous plume pulse and superswell events. *Gondw. Res.* **79**, 125–139 (2020).

85. R. D. Müller, M. Seton, S. Zahirovic, S. E. Williams, K. J. Matthews, N. M. Wright, G. E. Shephard, K. T. Maloney, N. Barnett-Moore, M. Hosseinpour, D. J. Bower, J. Cannon, Ocean basin evolution and global-scale plate reorganization events since pangea breakup. *Annu. Rev. Earth Planet. Sci.* **44**, 107–138 (2016).

86. N. A. Simmons, A. M. Forte, S. P. Grand, Thermochemical structure and dynamics of the African superplume. *Geophys. Res. Lett.* **34**, 2006GL028009 (2007).

87. J. Ritsema, H. J. van Heijst, J. H. Woodhouse, Complex shear wave velocity structure imaged beneath Africa and Iceland. *Science* **286,** 1925–1928 (1999).

88. T. H. Torsvik, B. Steinberger, G. E. Shephard, P. V. Doubrovine, C. Gaina, M. Domeier, C. P. Conrad, W. W. Sager, Pacific-panthalassic reconstructions: Overview, errata and the way forward. *Geochem. Geophys. Geosyst.* **20,** 3659–3689 (2019).

89. R. D. Müller, J. Cannon, X. Qin, R. J. Watson, M. Gurnis, S. Williams, T. Pfaffelmoser, M. Seton, S. H. J. Russell, S. Zahirovic, GPlates: Building a virtual earth through deep time. *Geochem. Geophys. Geosyst.* **19,** 2243–2261 (2018).